Check for updates

ADVANCED FUNCTIONAL MATERIALS
www.afm-journal.de

Tailored Micromagnet Sorting Gate for Simultaneous Multiple Cell Screening in Portable Magnetophoretic Cell-On-Chip Platforms

Jonghwan Yoon, Yumin Kang, Hyeonseol Kim, Abbas Ali, Keonmok Kim, Sri Ramulu Torati, Mi-Young Im, Changyeop Jeon, Byeonghwa Lim, and CheolGi Kim**

Conventional magnetophoresis techniques for manipulating biocarriers and cells predominantly rely on large-scale electromagnetic systems, which is a major obstacle to the development of portable and miniaturized cell-on-chip platforms. Herein, a novel magnetic engineering approach by tailoring a nanoscale notch on a disk micromagnet using two-step optical and thermal lithography is developed. Versatile manipulations are demonstrated, such as separation and trapping, of carriers and cells by mediating changes in the magnetic domain structure and discontinuous movement of magnetic energy wells around the circumferential edge of the micromagnet caused by a locally fabricated nano-notch in a low magnetic field system. The motion of the magnetic energy well is regulated by the configuration of the nanoscale notch and the strength and frequency of the magnetic field, accompanying the jump motion of the carriers. The proposed concepts demonstrate that multiple carriers and cells can be manipulated and sorted using optimized nanoscale multi-notch gates for a portable magnetophoretic system. This highlights the potential for developing cost-effective point-of-care testing and lab-on-chip systems for various single-cell-level diagnoses and analyses.

1. Introduction

The paradigm of modern medicine is transitioning from focusing on diagnosis for treatment to prioritizing diagnosis for prevention and prognosis, which has increased the importance of point-of-care testing (POCT).[1] In particular, cell diagnostics has become an emerging field because it can provide insights into the pathogenesis and prognosis of various diseases.[2] As miniaturized and portable analytical systems continue to gain significance in POCT, researchers are exploring the integration of lab-on-a-chip (LOC) systems to simplify the peripheral instruments for diagnosis at cell levels.[3] By combining POCT and LOC technologies, portable devices have the potential to facilitate the selective detection of bioactive substances, analyze drug responsiveness, and monitor cellular behavior in real time at the single-cell level. Cell-on-chip technology is being developed to be user-friendly and accessible, even for individuals without technical expertise. Researchers have explored various techniques in cell diagnosis, such as enzyme-linked immunosorbent assay involving antigen-antibody binding technology,[4] filter technology using microfilters[5] and micropores[6] in microfluidic structures, electrophoresis,[4b,7] Dielectrophoresis,[8] acoustophoresis,[9] and magnetophoresis,[10] to achieve portable cell analysis devices with high sensitivity and fast analysis speed. However, despite these advances, the ability to effectively manipulate individual cells is limited and remains a challenge for portable cellular analyses.

Magnetophoresis integrated with micromagnetic patterns is an attractive choice for designing individual cell manipulating techniques.[11] The micromagnetic patterns control the movement of micro-sized bio-carriers through the local magnetic energy. By arranging these patterns in a regular array, massive cells can be controlled simultaneously by merely applying an external magnetic field wirelessly. **Table 1** compares magnetophoretic approaches in terms of the magnetic field utilized, multidirectional transportation, gating function, simultaneous manipulation, and field generation methods. These methods offer efficient manipulation and sorting at the single-cell level, based on various

J. Yoon, Y. Kang, H. Kim, A. Ali, K. Kim, S. R. Torati[+], C. Jeon, C. Kim
Department of Physics and Chemistry
DGIST
Daegu 42988, Republic of Korea
E-mail: cgkim@dgist.ac.kr

M.-Y. Im
Center for X-ray Optics
Lawrence Berkeley National Laboratory
Berkeley, CA 94720, USA

B. Lim
Department of Smart Sensor Engineering
Andong National University
Andong 36729, Republic of Korea
E-mail: limbh@anu.ac.kr

The ORCID identification number(s) for the author(s) of this article can be found under https://doi.org/10.1002/adfm.202312875

[+]Present address: Center for Bioelectronics, Old Dominion University, Norfolk, VA 23508, USA

© 2024 The Authors. Advanced Functional Materials published by Wiley-VCH GmbH. This is an open access article under the terms of the Creative Commons Attribution License, which permits use, distribution and reproduction in any medium, provided the original work is properly cited.

DOI: 10.1002/adfm.202312875

Table 1. Comparison of the different magnetophoretic approaches for carrier and cell manipulation. (EM: electromagnet, PM: permanent magnet).

Magnetic element	Magnetic field / Electric field	Multi-directional transport	Gating function	Simultaneous manipulation of bead and cell	Field generation	Reference
Multiferroic array	5 kOe / 0.8 MV m^{-1}	No	No	Multiple	EM	[15]
Micro coils	30 Oe	Yes	No	Few	EM	[16]
Magnetic conduits	100 Oe – 500 Oe	Yes	Yes	Multiple	EM	[17]
Magnetic rings	< 500 Oe	Yes	No	Multiple	EM	[18]
T&I-bars track	< 400 Oe	Yes	No	Few	EM	[19]
Tri-symmetric track	< 200 Oe	No	Yes	Multiple	EM	[20]
Curved track	< 100 Oe	Yes	Yes	Multiple	EM	[21]
	400 Oe	Yes	No	Multiple	EM	[22]
Parallel stripes	< 40 Oe	No	Yes	Multiple	EM	[23]
Microdisks	< 100 Oe	Yes	Yes	Multiple	EM	[11,12]
Notched microdisk	< 50 Oe	Yes	Yes	Multiple (≈2000[a])	PM	This work

[a] Simultaneous manipulation of beads and cells per mm^2 (Multiple: > 1000 cells mm^{-2}).

magnetic elements. Especially in disk-shaped micromagnet, the bio-carriers and cells rotate individually along the boundary and synchronize with an external rotating magnetic field. By designing desired array of microdisk configurations, versatile manipulation and autonomous gating functions can be demonstrated with programable manner and high throughput.

The microdisks exhibit randomly located multiple magnetic domain structures under magnetic fields lower than the saturation field. These multiple-domain structures can cause discontinuous changes in the magnetization, resulting in a local discontinuous movement of the magnetic energy well and interfering with the precise control of the driving force. Previous studies primarily utilize an electromagnet instrument to generate a high-strength of in-plane rotating magnetic field to operate micromagnets in a single-domain state.[11,24] In addition, electric current and 3D magnetic fields are also required to achieve stable control and selective cell sorting.[12,17,18,21] However, using the additional equipment and externally connected large-scale electromagnet instruments to generate field remains a barrier to developing a portable cell-on-chip platform for multiple cell screening. To tackle this challenge, it is imperative to develop techniques that effectively manipulate magnetic bio-carriers under low magnetic field conditions with simplified devices.

This study introduces a sophisticated engineering approach for selective cell sorting on a handheld chip with a minimized rotating magnetic field (**Figure 1a**). This approach involves tailored nano-microscale notches on disk-shaped permalloy micromagnets for selectively sorting the magnetic carriers. The magnetic carriers move along the disk-shaped micromagnet array simultaneously and transport toward the notched micromagnet where the separation occurs (Figure 1a). Here, as shown in Figure 1b, two-step lithography was used to effectively produce several sorting gates: first, disk micromagnets were patterned by photolithography. Second, the nano-microscale notched micromagnets were patterned at the desired position on the chip by aligning with the previously fabricated disk micromagnets using thermal scanning probe lithography with a high resolution of ≈100 nm.

Notches on the micromagnet induce irregular alterations in the configuration of its multiple magnetic domains. These localized changes subsequently modulate the discontinuous change in the magnetic potential energy landscape at a fixed position near the notch, inducing the jumping of magnetic carriers and enabling the gate function of a carrier bound to specific cells. Inspired by the discontinuous change in the magnetization process observed in the classic magnetic Barkhausen effect, we named these phenomena as a mesoscopic magnetic Barkhausen (MMB) effect by borrowing only the concept of the Barkhausen effect accompanying irregular magnetization caused by discontinuous wall motion. To validate the feasibility of our approach, we demonstrated the control of carriers in a low magnetic field with a simplified magnetic field generator, as shown in Figure S1a (Supporting Information). The control field generator was constructed using a motor-driven rotating Halbach-structured permanent magnet to obtain a uniform in-plane magnetic field within the sample area (Figure S3a, Supporting Information). Additionally, we assessed the performance of the fabricated separation circuit, as shown in Figure 1a, to demonstrate the effective separation of different cells.

For the device design, numerical simulations were performed to analyze the movement of magnetic beads in unnotched, and nano-microscale notched disk micromagnets with various notch sizes, as shown in Figure S1b (Supporting Information). The magnetic energy of the micromagnets was calculated and the dynamic motion of the magnetic beads was analyzed to optimize their separation parameters. As a result, the device could efficiently separate and collect various magnetic carriers even under low magnetic fields of 50 Oe or less and at frequencies of 0.3 Hz or lower. Moreover, the nanoscale notched disk micromagnet device could successfully separate and classify THP-1 and MCF-7 cells by labeling them with magnetic carriers. The successful integration of this technology into portable devices demonstrates its potential use in the POCT cell-on-chip applications.

© 2024 The Authors. Advanced Functional Materials published by Wiley-VCH GmbH

16163028, 2024, 27, Downloaded from https://onlinelibrary.wiley.com/doi/10.1002/adfm.202312875 by Daegu Gyeongbuk Institute Of, Wiley Online Library on [10/09/2024]. See the Terms and Conditions (https://onlinelibrary.wiley.com/terms-and-conditions) on Wiley Online Library for rules of use; OA articles are governed by the applicable Creative Commons License

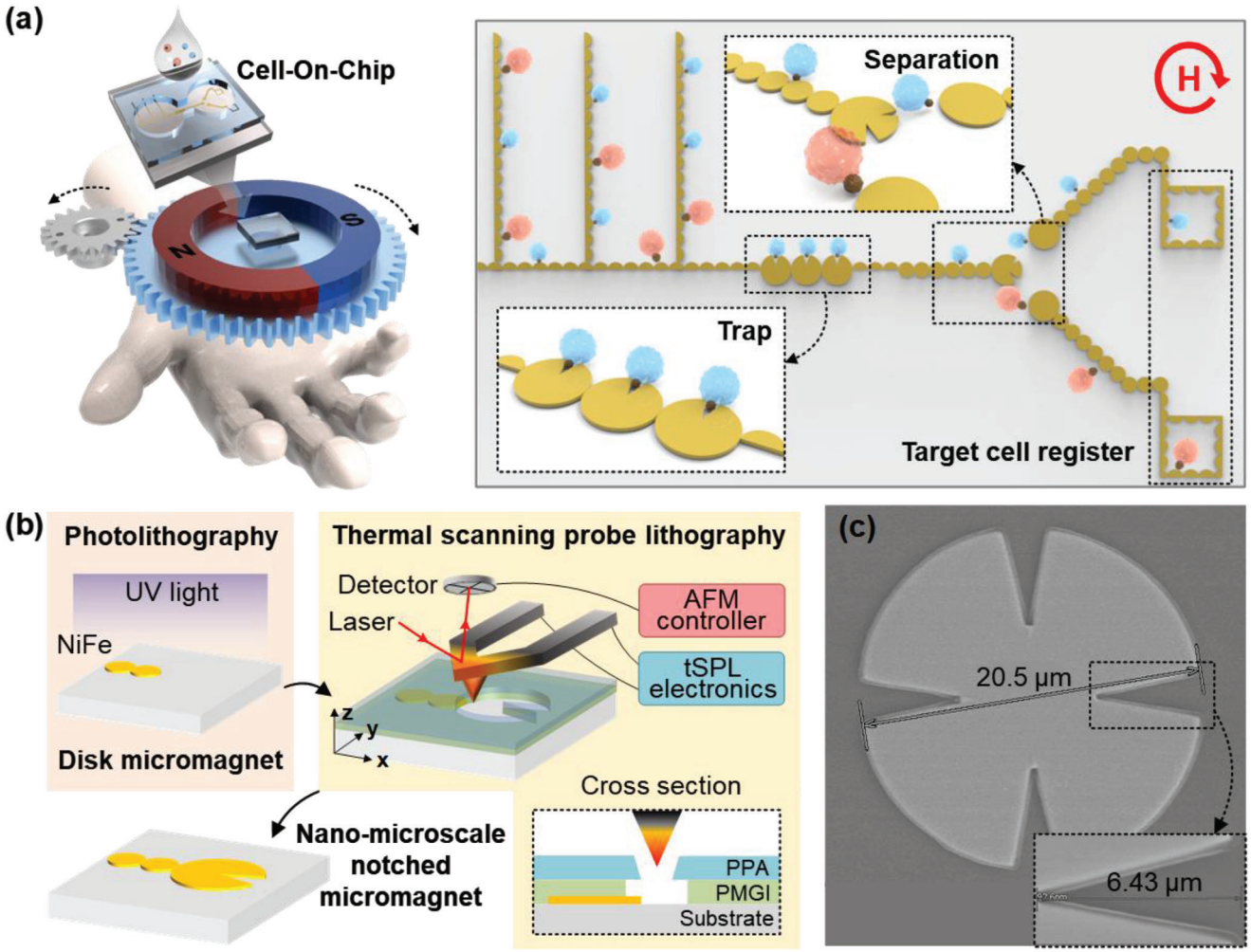

Figure 1. Overview of the portable magnetophoretic system for autonomous separation and delivery. a) The proposed cell-on-chip platform enables selective cell sorting and trapping with nano-microscale notched micromagnet. b) Engineering approach of UV optical and thermal scanning probe lithographies for micromagnet and nanoscale notches, respectively. c) SEM image depicting the fabricated notched micromagnet.

2. Results and Discussion

2.1. Induced MMB Effect by Tailoring Nanoscale Notches

To explain the dynamics of cell carriers, we have drawn upon the established concepts from previous classifications of magnetic carrier phase,[13] defining "phase lag" as the angular difference between the direction of the external magnetic field from the center of disk micromagnet and the carrier position. A carrier trapped in the energy well moved slower than the direction of the magnetic field owing to the liquid drag force. Under the rotating magnetic field, as the driving rotating frequency increased, the phase lag gradually increased. If the driving frequency exceeds a certain "critical frequency," the carrier experiences a repulsive force in the radial direction, causing it to jump from the micromagnet with an increased phase lag, referred to as the "phase-slipping mode." The phase lag, in which the transition from an attractive region to a repulsive region occurs, is called the "repulsive angle." Hence, the carriers were separated by jumping at the repulsive angle. As the frequency exceeded the critical threshold, the frequency of the rotating motion of the carrier around the micromagnet became zero, resulting in what is termed the "phase-isolation mode."

The nanoscale V-shaped notches were designed to have a specific depth on the disk micromagnet, which allowed the MMB effect to be induced at a low magnetic field that precisely controlled the repulsive angle. To analyze the dynamics of the carrier and the operating conditions is predicted by numerical simulations, the observed magnetic domains were compared with simulations to validate the magnetic states in the nano-microscale notched disk micromagnets. These domain variations were used to calculate the magnetic energy wells where the carriers were located.

To confirm the reliability of the simulation results, we designed a disk micromagnet with four nanoscale notches at 0°, 90°, 180°, and 270° with respect to the x-axis from the center of the micromagnet at varying notch depths. We used a $Ni_{80}Fe_{20}$ micromagnet with a radius of 2 μm and a thickness of 100 nm. The notch width was fixed at 200 nm, and the depths were 0.2, 0.6, 1, and 1.8 μm. The magnetic domains for 4 μm pattern were measured at a magnetic field strength of 50 Oe using magnetic

© 2024 The Authors. Advanced Functional Materials published by Wiley-VCH GmbH

16163028, 2024, 27, Downloaded from https://onlinelibrary.wiley.com/doi/10.1002/adfm.202312875 by Daegu Gyeongbuk Institute Of, Wiley Online Library on [10/09/2024]. See the Terms and Conditions (https://onlinelibrary.wiley.com/terms-and-conditions) on Wiley Online Library for rules of use; OA articles are governed by the applicable Creative Commons License

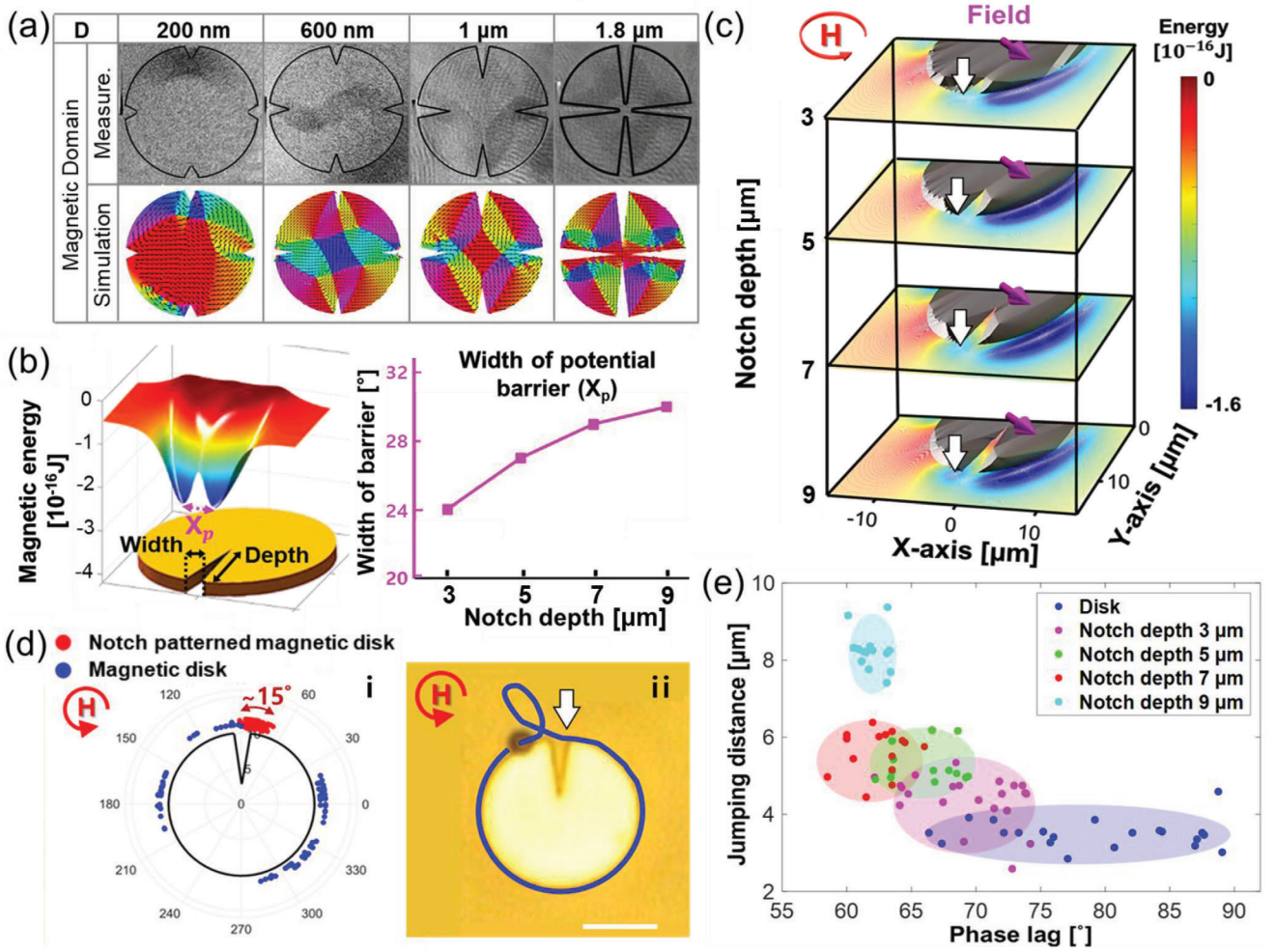

Figure 2. The magnetic domains for notched disk micromagnet and relationship with magnetic carrier dynamics. a) Observed magnetic domains and corresponding simulations under 50 Oe in-plane magnetic fields applied to quad-notched disk micromagnet with different depth(D). b) The variation of the energy barrier width (Xp) as a function of the notch depth in a disk micromagnet magnetized in the notch direction. Here, Xp is the angle between two minimum energy points of the barrier. c) Comparison of magnetic domain simulation and energy landscape according to notch depth when the angle of the 40 Oe in-plane magnetic field at 135° (Purple arrow). d) Comparison of jumping carrier locations between the disk micromagnet (blue) and notched disk micromagnet (red) over 20 rotation cycles of the magnetic field. The jumping position is the angle where the carrier is completely separated from the micromagnets (indicated by the white arrow in ii). The distribution of red dots is narrow near the notch. e) Variation of phase lag and jumping distance of magnetic carriers during 20 cycles of external magnetic field rotation, shown with different colors according to the notch depth.

transmission X-ray microscopy (MTXM),[14] the configurations of which matched well with simulated results under identical conditions, as compared in **Figure** 2a. All the parameters in the simulations were the same as those used in the experiments.

As shown in Figure 2b, we calculated the magnetic energy distribution with a single domain for different notches. When the notch direction was 90°, the magnetic energy formed a local energy barrier centered at 90°, creating two energy wells. The width (X_p) of the energy barrier increases with notch depth. Figure 2c shows the magnetic energy distribution calculated from the simulated magnetic domains when the magnetic field was applied at 135°. From the calculated magnetic energy, it can be observed that the depth of the energy well (marked by the white arrow) increased as the depth of the notch increased.

Generally, it is assumed that a carrier is situated at the local energy well. However, if the barrier is sufficiently small compared to the carrier size, the carrier can hop over the barrier. Therefore, when the carrier approached the notch in the magnetic well, indicated by the white arrow, the small carrier was unable to overcome the barrier. The well crossed the notch when it reached the repulsive angle in the radial direction, resulting the MMB effect. However, if the carrier is large, it can be expected to cross the well and be located in the lower energy well on the opposite side.

Figure 2d shows the tracking of the motion of carriers with 2.8 μm diameter along a 20 μm diameter unnotched disk during 20 cycles under a magnetic field of 20 Oe at a rotational frequency of 0.25 Hz. Phase slipping can cause carrier jumps in unnotched disk micromagnets at random locations as indicated by the blue dots in Figure 2d. However, from the above energy simulation results, it is evident that the influence of the energy barrier at the notch could identify the repulsive angle, thereby limiting the occurrence of the carrier jumping at the notch rather than at

© 2024 The Authors. Advanced Functional Materials published by Wiley-VCH GmbH

16163028, 2024, 27, Downloaded from https://onlinelibrary.wiley.com/doi/10.1002/adfm.202312875 by Daegu Gyeongbuk Institute Of, Wiley Online Library on [10/09/2024]. See the Terms and Conditions (https://onlinelibrary.wiley.com/terms-and-conditions) on Wiley Online Library for rules of use; OA articles are governed by the applicable Creative Commons License

random locations. The jumping locations of the carriers were located in the notches, as indicated by the red dots. Here, the blue dots appear randomly at wide angles, whereas the red dot distribution is narrow owing to the MMB effect near the notch, with an angle range of 15°.

We conducted repeated experiments with varying notch depths to observe changes in the angle and height of the jump of the carrier. The jump angle is defined as the phase lag at which the jump starts, and the jump height is defined as the shortest distance between the micromagnet and carrier. As shown in Figure 2e, the range of the jump angle decreased, and the jump distance increased as the depth of the notch increased. This is because the deeper the notch, the stronger the magnetic field gradient at the notch edge, which is necessary for the MMB effect. For the unnotched disk micromagnet, the jump distance and angle (indicated in blue in Figure 2e) were ≈ 2–3 times smaller and 5–6 times wider, respectively, than that of the 9 μm single-notched micromagnet indicated in red. These results suggest that by tailoring the nanoscale notch, it is possible to control the position and distance of jumps, even under low magnetic field conditions where multiple domains exist.

2.2. Regulation of Carrier Motion on Notched Micromagnet

To accurately tailor the notch, it is necessary to analyze the dynamics of the carrier using notch parameters. In the previous section, we assumed that the carriers were located at the minimum energy point of the well. However, a moving carrier is affected not only by the magnetic force, but also by the viscosity of the fluid. The viscous force was proportional to the relative velocity between the carrier and the fluid. Therefore, as the frequency of the rotating magnetic field increased, the viscous force increased, repelling the carrier from the minimum energy point until it reached the point where the magnetic and viscous forces were balanced. The critical frequency of the carrier is determined by the viscosity of the fluid and the magnetic field strength. In addition, the notch depth may affect the critical frequency because the size of the energy barrier depends on notch depth.

To investigate the critical frequency variations of carriers with diameters of 2.0 μm at different notch depths (3, 5, and 7 μm) we observed the movement of the carriers while varying the magnetic field strength and frequency. **Figure** 3a shows the critical frequency for a notch width and depth of 3 μm and 3 μm, respectively. If the driving frequency exceeded the critical frequency, intermittent jumping occurred, causing the carrier motion to enter the phase-slipping mode. Furthermore, as the magnetic field frequency increased, the frequency of the carriers reached 0 Hz, leading to a phase-isolation mode.

The critical frequency of the unnotched disk micromagnet increased proportionally with magnetic field strength. However, in the notched disk micromagnet, the critical frequency decreased from 30 Oe and reached 0 Hz between 50 and 60 Oe, indicating anomalous phase slipping (Figure 3b). As the notch depth increased, the critical frequency decreased, prompting a quicker transition to the anomalous phase-slipping mode and, correspondingly, a faster recovery. Above 70 Oe, the critical frequency increases rapidly and became similar to that of the unnotched disk.

As shown in Figure 3c and Movie S1 (Supporting Information), the movement of a 2.8 μm diameter carrier, which is smaller than the notch width, can be classified into three types: Type 1, where a carrier enters the notch along the boundary of the micromagnet and is trapped, showing the phase-locked mode; Type 2, where the carrier jumps near the notch; and Type 3, where the carrier enters the notch and subsequently exits. The jump height was zero or greater, depending on the magnetic field strength. When the jump height was zero, it was classified as Type 2-1, and when it was greater than zero, it was classified as Type 2-2, showing an anomalous phase-slipping mode. At a magnetic field strength of 10 Oe, when the notch width was within the range of 3 to 3.5 μm, the carrier moved in accordance with Type 1. When the width became 5 μm, it aligned with Type 2-1, and when it reached 7 μm, it demonstrated behavior characteristic of Type 2-2 (Figure S2, Supporting Information).

The simulation results in Figure 3c show that several small magnetic domains (white and black) nucleated near the notch in a weak magnetic field. This results in the formation of irregular large- and small-magnetic-energy wells. During the rotation of the magnetic field, the energy well closest to the carrier shifted toward the inside of the notch, trapping the carrier within the notch (Type 1). As the magnetic field strength increased, the divided magnetic domains merged, transforming the energy well across the notch into a wider shape on the opposite side, indicative of Type 2. In these cases, the carrier can jump from one side of the notch to the other. With further increase in the magnetic field, two energy wells were created near the notch, altering the direction and height of the jumps. This resulted in two types of jumps, Type 2-1 and Type 2-2. With the increase in magnetic field strength, the magnetic domains merged, and a narrow energy well was formed along the notch boundary. Thus, the carrier could pass around the periphery of the notch edge and exhibited Type 3 behavior.

2.3. Sorting Gate Efficiency Depending on Various Operation Parameters

According to the classified motion types of the tailor notched micromagnet, the micromagnets can perform the separating function even under low magnetic field strength and frequency operating conditions, which are optimized for activating the jump of carriers of a specific size. The jumping movement of the carrier under the Type 2-2 conditions was analyzed to optimize the separation gate. **Figure** 4a shows the distribution of the jump distance and angle according to different carrier sizes for 15 cycles. The critical frequency is 0.2 Hz or less. Regardless of the carrier size, a jump appears around the notch. It jumps higher for smaller carriers. Moreover, the deeper the notch depth, the higher the jump distance. Overall, the probability of the jumping distance distribution for different notch depths was measured, as shown in Figure 4b.

For parameter optimization, the phase diagrams of the magnetic carrier movement types were classified according to the magnetic field strength and carrier size, as shown in Figure 4c. The region where the micromagnet can operate as a separation element under Type 2-2 mode is marked as the green region. The three different size ranges of the carriers demonstrate the

© 2024 The Authors. Advanced Functional Materials published by Wiley-VCH GmbH

16163028, 2024, 27, Downloaded from https://onlinelibrary.wiley.com/doi/10.1002/adfm.202312875 by Daegu Gyeongbuk Institute Of, Wiley Online Library on [10/09/2024]. See the Terms and Conditions (https://onlinelibrary.wiley.com/terms-and-conditions) on Wiley Online Library for rules of use; OA articles are governed by the applicable Creative Commons License

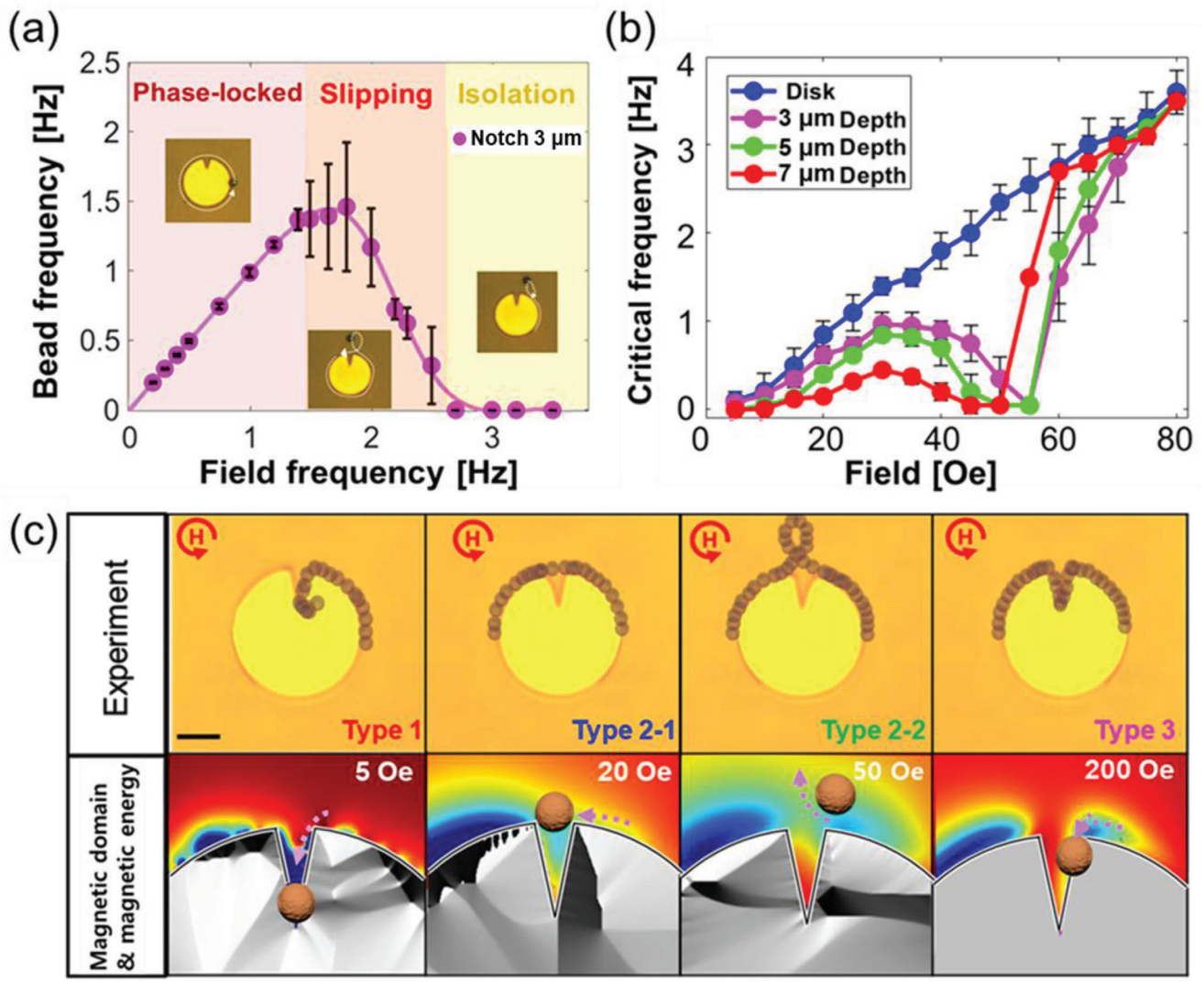

Figure 3. Regulation of magnetic carrier motion facilitated by notched disk micromagnet. a) Frequency variation for a micromagnet with a 3 μm notch width and 3 μm depth, using 2.0 μm magnetic carriers in response to increased magnetic field frequency. The field intensity is 40 Oe, and the size of the micromagnet is a diameter of 20 μm. b) The critical frequency variation of magnetic carriers in response to the strength of a magnetic field is presented as a function of notch depths under the same conditions. Anomalous phase isolation between 30 and 60 Oe for the notched disk is observed. c) Comparison of magnetic domain shape and magnetic energy distribution around the notch and the measured movement of magnetic carriers smaller than the notch width for different magnetic field strengths. The scale bar is 5 μm. The notch width is 3 μm, and the depth is 5 μm.

manifestation of the Type 2-2 mode under a particular notch condition. Accordingly, the operating range of the magnetic field and the optimized parameters of the notches were selected to realize a high gating efficiency in a low magnetic field suitable for hand-carrying.

2.4. Simultaneous Separation of Different Types of Live Cells in POCT Platform

For the POCT system under the sorting conditions analyzed, a weak magnetic field generation system was constructed by arranging NdFeB permanent magnets in a Halbach structure mounted in a printed mold using an FDM 3D printer. The Halbach structure was designed by magnetic field simulations using ANSYS Maxwell to obtain a uniform magnetic field of 15–60 Oe. Based on FEMM 3.0 Software, the magnetic field distribution form the Halbach array magnets provides a high uniformity within the sample area (Figure S3b, Supporting Information). Furthermore, we fabricated the body using an FDM 3D printer, and the rotation controlled the speed and direction of the motor using an Arduino. As a result of the measurement, the magnetic carriers were successfully separated depending on their size (Figure S3b, Supporting Information), which confirmed that carriers or cells could be separated using a simple permanent magnet system instead of a rotating magnetic field by 2D-electromagnet.

Under an optimized magnetic field strength of 40 Oe and frequency of 0.2 Hz, a multi-notched disk micromagnet for separation gate element was developed for separating magnetic car-

© 2024 The Authors. Advanced Functional Materials published by Wiley-VCH GmbH

16163028, 2024, 27, Downloaded from https://onlinelibrary.wiley.com/doi/10.1002/adfm.202312875 by Daegu Gyeongbuk Institute Of, Wiley Online Library on [10/09/2024]. See the Terms and Conditions (https://onlinelibrary.wiley.com/terms-and-conditions) on Wiley Online Library for rules of use; OA articles are governed by the applicable Creative Commons License

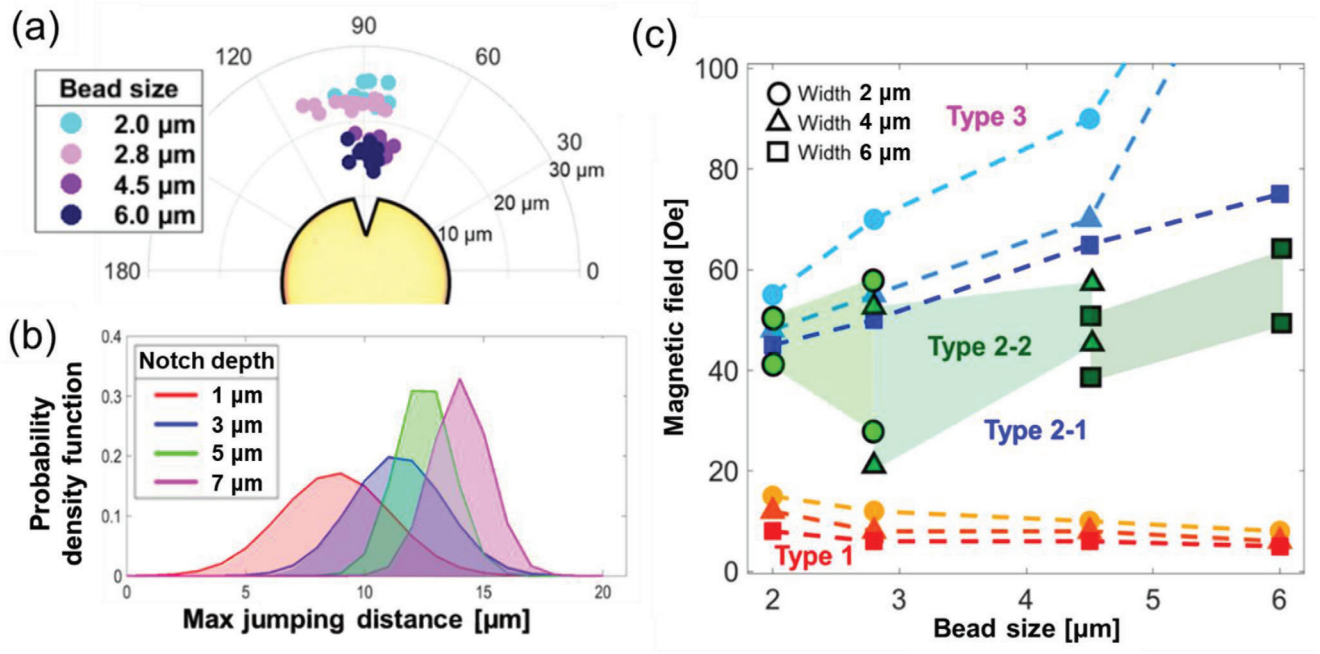

Figure 4. Separation conditions for the different sizes of magnetic carriers in notched disk micromagnets. a) Jump distribution according to the size of the magnetic carrier on a notched disk micromagnet with 5 μm depth under Type 2-2 conditions. b) Jump probability distribution of 2.8 μm magnetic carrier according to notch depth under Type 2-2 conditions. c) A phase diagram depicting a magnetic carrier's motion influenced by notch width (3 μm, 5 μm, and 7 μm) and magnetic field strength. The carrier jumping for Type 2-2 in the diagram represents the operation parameters of a speed of 0.2 Hz or less and a jump distance exceeding 7.5 μm (colored region).

riers with diameters of 2.8 and 4.5 μm, and the sorting performance was demonstrated as shown in **Figure 5**. The jumping gate element was designed with a 5 μm depth, 1.5 μm wide notch, and a 9 μm depth, 3.5 μm wide notch. Three sets of carriers with diameters of 2.8, 4.5, and 6.0 μm, respectively, were loaded onto the fabricated device, which included an array of unnotched micromagnets and a gate element. First, the carriers with a diameter of 2.8 μm were separated into Route I. Second, the carriers with a diameter of 4.5 μm were sorted into Route II through jumping. Finally, the remaining largest carriers moved to Route III without employing jumping (Movie S2, Supporting Information).

Moreover, the cells were labeled with magnetic carriers, and autonomous separation according to the cell type was demonstrated (Movie S2, Supporting Information). THP-1 and MCF-7 cells were labeled with 2.8 μm and 6.0 μm diameter of carriers, respectively. As shown in Figure 5a, under the optimized operating conditions of 40 Oe field strength and 0.2 Hz frequency, the multi-notched disk micromagnet enabled the separation of the two types of cells in different directions. The isolated cells were identified using bright-field and fluorescence imaging (Figure 5b).

3. Conclusion

A multi-notched disk micromagnet was developed to enable the versatile manipulation of magnetic carriers and cells, even in a low magnetic field, which is suitable for a POCT systems. In existing magnetophoretic circuits, if the applied magnetic field is weaker than the saturation field, the micromagnet reveals multiple domains, making precise manipulation of the magnetic carriers challenging. However, the multi-notched disk micromagnet overcomes this difficulty by enabling various manipulations of magnetic carriers, such as separation, capture, and delay, even in weaker and slower rotating magnetic fields. By integrating this device with field generation using the Halbach structure of a permanent magnet assembly, many carriers can be controlled in a smaller area, expanding its applicability across versatile range of systems. This technology enables the separation and precise control of individual cells, even with a small magnetic field generator using a permanent magnet, which is a significant milestone for the further development and implementation of next-generation POCT and Cells-on-Chip technology. Overall, this technology holds the potential to revolutionize rapid cell analysis by providing a simple, cost-effective, and efficient solution for analyzing bioactive substances and cells.

4. Experimental Section

External Magnetic Field: Four ferrite-core solenoid coils produced a rotating in-plane magnetic field within the x–y plane. The strength and frequency of the rotating magnetic field were controlled using LabVIEW software. A magnetic field was applied to the POCT magnetophoretic system using a Halbach array field generator composed of NdFeB permanent magnets and a holder fabricated using an FDM 3d printer, as shown in Figure S3a (Supporting Information). A 5×5 mm (diameter and thickness) stick-type NdFeB magnet was used from HB magnet as the Nd permanent magnet. ANSYS Maxwell software was used to confirm that the magnetic field was generated uniformly in the Halbach array structure. The rotational magnetic field generator was comprised of a gear holder

© 2024 The Authors. Advanced Functional Materials published by Wiley-VCH GmbH

16163028, 2024, 27, Downloaded from https://onlinelibrary.wiley.com/doi/10.1002/adfm.202312875 by Daegu Gyeongbuk Institute Of, Wiley Online Library on [10/09/2024]. See the Terms and Conditions (https://onlinelibrary.wiley.com/terms-and-conditions) on Wiley Online Library for rules of use; OA articles are governed by the applicable Creative Commons License

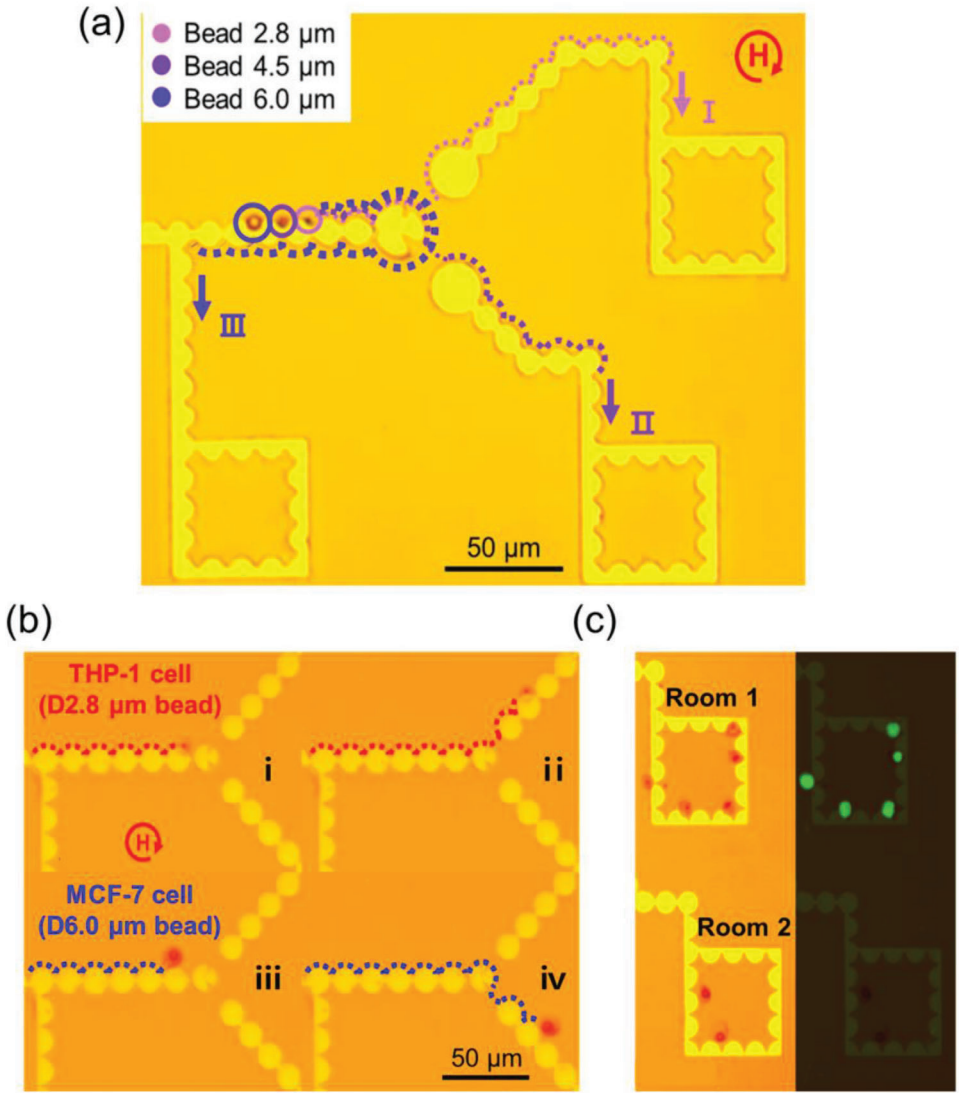

Figure 5. Autonomous separation of carriers and simultaneous separation of THP-1 and MCF-7 cells using POCT system with Halbach-structured magnet assembly. a) The separation of three sizes of magnetic carriers (2.8, 4.5, 6.0 μm) to the individual room performed by the 2 types of notched disk micromagnet devices. Here, upper notches are 5 μm deep and 3 μm wide, while lower notches are 7 μm deep and 6 μm wide. b) Simultaneous separation of THP-1 and MCF-7 cells. The separation of living THP-1 and MCF-7 cells was tested using a multi-notched disk micromagnet device in a cell culture environment (10% FBS RPMI medium). The trajectory of live THP-1 and MCF-7 cells on the multi-notched disk micromagnet device (i–iv) was observed. They were separated into individual compartments under the rotating field of 40 Oe at 0.2 Hz. c) Bright-field and fluorescent images of the trapped THP-1 and labeled MCF-7 cells stained with green fluorescence dye in the individual apartments.

crafted with a 3D printer and enables mechanical rotation, a rotating motor, and an Arduino chip responsible for controlling the rotation of the motor.

Nanoscale Notched Micromagnet and Array Preparation: Two-step lithography techniques were employed to fabricate the micromagnets. Photolithography techniques were primarily used to pattern the microstructures for most micromagnet fabrication. Furthermore, as shown in Figure S4a (Supporting Information), a one-step thermal scanning probe lithography was developed (t-SPL) technique to fabricate nanoscale notches on micromagnets and micromagnet arrays. The fabrication of micromagnets other than notched disk micromagnets has also been reported. Photolithography and direct-current magnetron sputtering were used to produce an array of micromagnets of a $Ni_{80}Fe_{20}$ thin film (thickness: 100 nm) on a Si substrate.

For the fabrication process of the notched disk micromagnet cases, a solution of pure PMGI-SF4 (polymethylglutarimide, Sigma) was spin-coated on the surface of the sample (2000 rpm at 500 rpm s^{-1} for 45 s) followed by a quick baking (200 °C for 1 min). Subsequently, a PPA (polyphthalaldehyde, Sigma) solution (1.3 wt % in anisole) was spin-coated onto PMGI (3000 rpm at 500 rpm s^{-1} for 60 s) followed by a quick baking (90 °C for 3 min). Under these conditions, a 30 nm thick PPA film was deposited on top of a 155 nm thick PMGI film on the sample surface. PPA patterning was achieved using a commercial t-SPL (NanoFrazor, SwissLitho AG), equipped with tips ranging in radius from 20 to 100 nm. The tips, selected for their high thermal transport and capability for high-resolution line widths exceeding 100 nm, were heated to ≈ 950 °C for patterning. The writing process involved heating the tips above 150 °C at the 2D/PPA surface and contacting them from a height of ≈ 300 nm between the sample

© 2024 The Authors. Advanced Functional Materials published by Wiley-VCH GmbH

16163028, 2024, 27, Downloaded from https://onlinelibrary.wiley.com/doi/10.1002/adfm.202312875 by Daegu Gyeongbuk Institute Of, Wiley Online Library on [10/09/2024]. See the Terms and Conditions (https://onlinelibrary.wiley.com/terms-and-conditions) on Wiley Online Library for rules of use; OA articles are governed by the applicable Creative Commons License

16163028, 2024, 27, Downloaded from https://onlinelibrary.wiley.com/doi/10.1002/adfm.202312875 by Daegu Gyeongbuk Institute Of, Wiley Online Library on [10/09/2024]. See the Terms and Conditions (https://onlinelibrary.wiley.com/terms-and-conditions) on Wiley Online Library for rules of use; OA articles are governed by the applicable Creative Commons License

and the cantilever. The CAD program-drawn pattern image was divided into a 20 × 20 nm mesh using NanoFrazor Software.

Post-patterning, samples were immersed in a solution of TMAH in deionized water (tetramethylammonium hydroxide AZ726 MIF, MicroChemicals) (0.17 mol L^{-1}) for 155 s, then rinsed with deionized water (30 s) and Isopropyl alcohol (30 s), and finally dried with N_2. Metal deposition was performed using DC magnetron sputtering along with other micromagnet fabrication methods. Liftoff was performed by dipping the samples in Remover PG (MicroChem) for a few hours, followed by rinsing (methanol) and drying using N_2. A Teflon film (500 nm) was then coated to reduce surface adhesion between the carriers and cells. A notched disk micromagnet fabricated using the t-SPL was shown in Figure S4b (Supporting Information). As shown in Figure S4c (Supporting Information), it was manufactured with a resolution of 90 nm minimum line width. For the array micromagnets, excluding the notched disk micromagnets, manufacturing was based on photolithography. Subsequently, notched disk micromagnets were aligned at the correct location using Nanofrazer equipment, as shown in Figure S4d (Supporting Information).

Magnetic Domain and Field Observation and Simulation: The Micromagnet patterns were fabricated on X-ray transparent SiN membranes using e-beam lithography and sequential liftoff processes for magnetic domain observation. A magnetic film ($Ni_{80}Fe_{20}$, 100 nm thickness) was deposited by DC magnetron sputtering. The domain structures were observed using full-field MTXM at the Advanced Light Source (XM-1, Beamline 6.1.2), with a high spatial resolution of 25 nm, where the X-ray magnetic circular dichroism mechanism provides magnetic contrast. The photon energy was set to the Fe L3 (707 eV). To enhance the magnetic contrast and eliminate the nonmagnetic background, images captured at specific fields were normalized to an image recorded in a saturation state. To observe the entire domain structures of the micromagnets, the 2D size of the notched disk micromagnets (4 µm diameter) were downscaled owing to the beam size limitation of MTXM.

In contrast, micromagnetic domain and field simulations and magnetic carrier manipulation were conducted using MuMax3 software. The parameters were set up with an exchange stiffness Aex = 1.0×10^{-11} J m^{-1}, saturation magnetization Ms = 800 kA m^{-1}, damping constant $\alpha = 0.1$, zero magnetocrystalline anisotropy as standard material parameters. The cell dimensions of the 4 µm diameter notched micromagnets were 5 × 5 × 20 nm^3, and the cell dimensions of 20 µm diameter notched micromagnets were 20 × 20 × 100 nm^3 (Figure S5, Supporting Information). The magnetostatic potential energy of a spherical superparamagnetic particle the magnetostatic potential energy of a spherical superparamagnetic particle with linear volumetric susceptibility, χ_v, in a space- and time-varying magnetic field B was given by:[11]

$$U\left(\vec{r},t\right) = -\frac{1}{2}\frac{\chi_v V}{\mu_0}\vec{B}^2 \quad (1)$$

where V was the volume of the particle, $\mu_0$was the vacuum permeability, and $B = B_{ext} + B_{sub}$ was the total magnetic field generated at the particle center, which was the sum of a uniform rotating external field, B_{ext}(t), and a space–time-varying substrate field, B_{sub} (r, t). The magnetic potential energy was numerically calculated using MATLAB R2021b based on the simulated field.

Cells Culture and Superparamagnetic Carriers Binding: THP-1 (ATCC, TIB-202) cells and MCF-7 (ATCC, HTB-22) cells were cultured in RPMI 1640 medium (Gibco, 11875-085) and DMEM (Gibco, 12430-054) supplemented with 10% FBS and 1% penicillin/streptomycin. Two types of antibodies, HLA-A2 and EpCAM, were used to label THP-1 and MCF-7 cells, respectively, with magnetic carriers. Each antibody solution (0.5 g L^{-1}) and Biotin-PEG-NHS linker solution (1 g L^{-1}) was mixed using a vortex rotator for 1 h to obtain biotinylated antibodies. The solution was filtered using spin-desalting columns to remove unbound linkers. Streptavidin-coated magnetic carriers (2.8 µm diameter) (M-280; Invitrogen, Grand Island, NY, USA) were bound with biotinylated antibodies. The carriers were then washed with PBS (pH 7.4). Each biotinylated antibody was added to 5 µL of the carrier solution at a final antibody concentration of 3×10^{-6} g mL^{-1}. The solution was thoroughly mixed using a vortex rotator at room temperature for 1 h. The carriers were washed several times with PBS (0.02% Tween-20) using a magnet to remove the unbound antibodies. Finally, the antibody-bound carriers were resuspended in PBS (0.5 mL) and stored at 4°C for further use.

Supporting Information

Supporting Information is available from the Wiley Online Library or from the author.

Acknowledgements

J.Y., Y.K. contributed equally to the work. This research was supported by the National Research Foundation of Korea (NRF) grant funded by the Korean Government (MSIT) (2018R1A5A1025511). The work at ALS was supported by the Director, Office of Science, Office of Basic Energy Sciences, Scientific User Facilities Division of the US Department of Energy, under Contract No. DE-AC02-05CH11231.

Conflict of Interest

The authors declare no conflicts of interest.

Data Availability Statement

The data that support the findings of this study are available on request from the corresponding author. The data are not publicly available due to privacy or ethical restrictions.

Keywords

lab-on-a-chip, magnetophoresis, micromagnet, single-cell analysis, single-cell manipulation

Received: October 18, 2023
Revised: January 29, 2024
Published online: March 5, 2024

[1] a) P. Yager, G. J. Domingo, J. Gerdes, *Annu. Rev. Biomed. Eng.* **2008**, *10*, 107; b) H. Geng, S. Vilms Pedersen, Y. Ma, T. Haghighi, H. Dai, P. D. Howes, M. M. Stevens, *Acc. Chem. Res.* **2022**, *55*, 593; c) L. Zhang, B. Ding, Q. Chen, Q. Feng, L. Lin, J. Sun, *TrAC Trends Anal. Chem.* **2017**, *94*, 106; d) Z. Zhang, P. Ma, R. Ahmed, J. Wang, D. Akin, F. Soto, B.-F. Liu, P. Li, U. Demirci, *Adv. Mater.* **2022**, *34*, 2103646; e) J. Dinnes, P. Sharma, S. Berhane, S. S. van Wyk, N. Nyaaba, J. Domen, M. Taylor, J. Cunningham, C. Davenport, S. Dittrich, D. Emperador, L. Hooft, M. M. G. Leeflang, M. D. F. McInnes, R. Spijker, J. Y. Verbakel, Y. Takwoingi, S. Taylor-Phillips, A. Van den Bruel, J. J. Deeks, *Cochrane Database Syst. Rev.* **2022**, *7*, CD013705.

[2] P. Raghavendra, T. Pullaiah, in *Advances in Cell and Molecular Diagnostics*, Academic Press, Cambridge **2018**.

[3] a) Y. Xiao, S. Li, Z. Pang, C. Wan, L. Li, H. Yuan, X. Hong, W. Du, X. Feng, Y. Li, P. Chen, B.-F. Liu, *Biosens. Bioelectron.* **2022**, *206*, 114130; b) H. Yuan, P. Chen, C. Wan, Y. Li, B.-F. Liu, *TrAC Trend Anal. Chem.* **2022**, *157*, 116814; c) H. Tavakoli, S. Mohammadi, X. Li, G. Fu, X. Li, *TrAC Trend. Anal. Chem.* **2022**, *157*, 116806; d) A. K. Yetisen, M. S. Akram, C. R. Lowe, *Lab Chip* **2013**, *13*, 2210; e) Z. Li, Y. Bai, M. You, J. Hu, C. Yao, L. Cao, F. Xu, *Biosens. Bioelectron.* **2021**, *177*, 112952; f) A. Kumar, A. Parihar, U. Panda, D. S. Parihar, *ACS Appl. Bio Mater.* **2022**, *5*, 2046.

© 2024 The Authors. Advanced Functional Materials published by Wiley-VCH GmbH

[4] a) D. Liu, X. Li, J. Zhou, S. Liu, T. Tian, Y. Song, Z. Zhu, L. Zhou, T. Ji, C. Yang, *Biosens. Bioelectron.* **2017**, *96*, 332; b) F.-Z. Kong, S. Jahan, R. Zhong, X.-Y. Cao, W.-L. Li, Y.-X. Wang, H. Xiao, W.-W. Liu, C.-X. Cao, *ACS Sens.* **2019**, *4*, 126; c) L. Beaudet, R. Rodriguez-Suarez, M.-H. Venne, M. Caron, J. Bédard, V. Brechler, S. Parent, M. Bielefeld-Sévigny, *Nat. Methods* **2008**, *5*, an8; d) Y. Wang, X. Liu, C. Chen, Y. Chen, Y. Li, H. Ye, B. Wang, H. Chen, J. Guo, X. Ma, *ACS Nano* **2022**, *16*, 180; e) S. Wang, S. Tasoglu, P. Z. Chen, M. Chen, R. Akbas, S. Wach, C. I. Ozdemir, U. A. Gurkan, F. F. Giguel, D. R. Kuritzkes, U. Demirci, *Sci. Rep.* **2014**, *4*, 3796; f) S. Ghosh, K. Aggarwal, V. T. U, T. Nguyen, J. Han, C. H. Ahn, *Microsyst. Nanoeng.* **2020**, *6*, 5.

[5] B. Xu, J. Zhang, D. Pan, J. Ni, K. Yin, Q. Zhang, Y. Ding, A. Li, D. Wu, Z. Shen, *Lab Chip* **2022**, *22*, 4382.

[6] W. Liu, Y. Deng, Y. Yuan, S. L. Ouyang, Q. Liu, X. Chen, *ACS Appl. Mater. Interfaces* **2023**, *15*, 21690.

[7] a) M. N. Hasan, A. Fraiwan, R. An, Y. Alapan, R. Ung, A. Akkus, J. Z. Xu, A. J. Rezac, N. J. Kocmich, M. S. Creary, T. Oginni, G. M. Olanipekun, F. Hassan-Hanga, B. W. Jibir, S. Gambo, A. K. Verma, P. K. Bharti, S. Riolueang, T. Ngimhung, T. Suksangpleng, P. Thota, G. Werner, R. Shanmugam, A. Das, V. Viprakasit, C. M. Piccone, J. A. Little, S. K. Obaro, U. A. Gurkan, *Analyst* **2020**, *145*, 2525; b) J.-Z. Pan, P. Fang, X.-X. Fang, T.-T. Hu, J. Fang, Q. Fang, *Sci. Rep.* **2018**, *8*, 1791.

[8] a) E.-S. Yu, H. Lee, S.-M. Lee, J. Kim, T. Kim, J. Lee, C. Kim, M. Seo, J. H. Kim, Y. T. Byun, S.-C. Park, S.-Y. Lee, S.-D. Lee, Y.-S. Ryu, *Nat. Commun.* **2020**, *11*, 2804; b) S. Park, Y. Zhang, T.-H. Wang, S. Yang, *Lab Chip* **2011**, *11*, 2893; c) X. Wang, Y. Xin, L. Ren, Z. Sun, P. Zhu, Y. Ji, C. Li, J. Xu, B. Ma, *Sci. Adv.* **2020**, *6*, eabb3521.

[9] a) K. P. P. R. Nair, T. C. P. Veettil, B. R. Wood, D. Paul, T. Alan, *Biosensors* **2022**, *12*, 119; b) K. Sun, H. Wang, L. Wang, Y. Lu, R. Liu, P. Liu, J. Cheng, *Lab Chip* **2021**, *21*, 933; c) D. J. Collins, B. Morahan, J. Garcia-Bustos, C. Doerig, M. Plebanski, A. Neild, *Nat. Commun.* **2015**, *6*, 8686; d) P. Dow, K. Kotz, S. Gruszka, J. Holder, J. Fiering, *Lab Chip* **2018**, *18*, 923; e) A. Ozcelik, J. Rufo, F. Guo, Y. Gu, P. Li, J. Lata, T. J. Huang, *Nat. Methods* **2018**, *15*, 1021; f) A. Riaud, W. Wang, A. L. P. Thai, V. Taly, *Phys. Rev. Appl.* **2020**, *13*, 034058.

[10] a) S. Knowlton, A. Joshi, P. Syrrist, A. F. Coskun, S. Tasoglu, *Lab Chip* **2017**, *17*, 2839; b) J. Kim, M. Jang, K. G. Lee, K.-S. Lee, S. J. Lee, K.-W. Ro, I. S. Kang, B. D. Jeong, T. J. Park, H.-J. Kim, J. Lee, *ACS Appl. Mater. Interfaces* **2016**, *8*, 23489; c) W. Zhao, R. Cheng, J. R. Miller, L. Mao, *Adv. Funct. Mater.* **2016**, *26*, 3916.

[11] a) S. R. Goudu, H. Kim, X. Hu, B. Lim, K. Kim, S. R. Torati, H. Ceylan, D. Sheehan, M. Sitti, C. Kim, *Nat. Commun.* **2021**, *12*, 3024; b) H. Kim, B. Lim, J. Yoon, K. Kim, S. R. Torati, C. Kim, *Adv. Sci.* **2021**, *8*, 2100532; c) H. Kim, J. Yoon, A. Ali, S. R. Torati, Y. Kang, K. Kim, B. Lim, C. Kim, *J. Sci.: Adv. Mater. Dev.* **2022**, *7*, 100482.

[12] a) B. Lim, V. Reddy, X. Hu, K. Kim, M. Jadhav, R. Abedini-Nassab, Y.-W. Noh, Y. T. Lim, B. B. Yellen, C. Kim, *Nat. Commun.* **2014**, *5*, 3846; b) X. Hu, S. R. Torati, H. Kim, J. Yoon, B. Lim, K. Kim, M. Sitti, C. Kim, *Small* **2019**, *15*, 1901105. c) J. Yoon, Y. Kang, H. Kim, S. R. Torati, K. Kim, B. Lim, C. Kim, *Adv. Sci.* **2022**, *9*, 2103579;

[13] X. Hu, R. Abedini-Nassab, B. Lim, Y. Yang, M. Howdyshell, R. Sooryakumar, B. B. Yellen, C. Kim, *J. Appl. Phys.* **2015**, *118*, 203904.

[14] a) X. Hu, S. R. Torati, H. Kim, J. Yoon, B. Lim, K. Kim, M. Sitti, C. Kim, *Small* **2019**, *15*, e1901105; b) M.-Y. Im, K.-S. Lee, A. Vogel, J.-I. Hong, G. Meier, P. Fischer, *Nat. Commun.* **2014**, *5*, 5620; c) H.-S. Han, S. Lee, S.-G. Je, M. Kang, H.-J. Ok, N. Kim, W. Chao, M.-Y. Im, K.-S. Lee, *ACS Appl. Nano Mater.* **2021**, *4*, 9912.

[15] R. Khojah, Z. Xiao, M. K. Panduranga, M. Bogumil, Y. Wang, M. Goiriena-Goikoetxea, R. V. Chopdekar, J. Bokor, G. P. Carman, R. N. Candler, D. Di Carlo, *Adv. Mater.* **2021**, *33*, 2006651.

[16] H. Lee, Y. Liu, D. Ham, R. M. Westervelt, *Lab Chip* **2007**, *7*, 331

[17] a) M. Donolato, P. Vavassori, M. Gobbi, M. Deryabina, M. F. Hansen, V. Metlushko, B. Ilic, M. Cantoni, D. Petti, S. Brivio, R. Bertacco, *Adv. Mater.* **2010**, *22*, 2706. b) E. Rapoport, D. Montana, G. S. D. Beach, *Lab Chip* **2012**, *12*, 4433. c) A. Torti, V. Mondiali, A. Cattoni, M. Donolato, E. Albisetti, A. M. Haghiri-Gosnet, P. Vavassori, R. Bertacco, *Appl. Phys. Lett.* **2012**, *101*, 141101. d) M. Donolato, A. Torti, N. Kostesha, M. Deryabina, E. Sogne, P. Vavassori, M. F. Hansen, R. Bertacco, *Lab Chip* **2011**, *11*, 2976.

[18] a) A. Sarella, A. Torti, M. Donolato, M. Pancaldi, P. Vavassori, *Adv. Mater.* **2014**, *26*, 2384. b) P. Vavassori, M. Gobbi, M. Donolato, M. Cantoni, R. Bertacco, V. Metlushko, B. Ilic, *J. Appl. Phys.* **2010**, *107*, 09B301.

[19] a) G. Katsikis, J. S. Cybulski, M. Prakash, *Nat. Phys.* **2015**, *11*, 588. b) R. Abedini-Nassab, S. Bahrami, *Lab Chip* **2021**, *21*, 1998

[20] U. Sajjad, E. Lage, J. McCord, *Adv. Mater. Interfaces* **2018**, *5*, 1801201.

[21] R. Abedini-Nassab, D. Y. Joh, M. A. Triggiano, C. Baker, A. Chilkoti, D. M. Murdoch, B. B. Yellen, *Adv. Funct. Mater.* **2016**, *26*, 4026.

[22] F. Block, F. Klingbeil, U. Sajjad, C. Arndt, S. Sindt, D. Seidler, L. Thormählen, C. Selhuber-Unkel, J. McCord, *Adv. Mater. Technol.* **2023**, *8*, 2300260.

[23] a) R. Huhnstock, L. Paetzold, M. Merkel, P. Kuświk, A. Ehresmann, *Small* **2023**, 2305675; b) R. Huhnstock, M. Reginka, A. Tomita, M. Merkel, K. Dingel, D. Holzinger, B. Sick, M. Vogel, A. Ehresmann, *Sci. Rep.* **2021**, *11*, 21794.

[24] a) A. Ali, H. Kim, S. R. Torati, Y. Kang, V. Reddy, K. Kim, J. Yoon, B. Lim, C. Kim, *Small* **2024**, *20*, 2305528; b) X. Hu, K. Kim, A. Ali, H. Kim, Y. Kang, J. Yoon, S. R. Torati, V. Reddy, M.-Y. Im, B. Lim, C. Kim, *Small Methods* **2024**, 2301495; b)c) H. Kim, Y. Kang, B. Lim, J. Yoon, A. Ali, S. R. Torati, C. Kim, *Mater. Horizons* **2022**, *9*, 2353.

© 2024 The Authors. Advanced Functional Materials published by Wiley-VCH GmbH

16163028, 2024, 27, Downloaded from https://onlinelibrary.wiley.com/doi/10.1002/adfm.202312875 by Daegu Gyeongbuk Institute Of, Wiley Online Library on [10/09/2024]. See the Terms and Conditions (https://onlinelibrary.wiley.com/terms-and-conditions) on Wiley Online Library for rules of use; OA articles are governed by the applicable Creative Commons License